

Received June 8, 2018, accepted June 19, 2018, date of current version August 20, 2018.

Digital Object Identifier 10.1109/ACCESS.2018.2860679

# Modeling and Integration of a Lithium-Ion Battery Energy Storage System With the More Electric Aircraft 270 V DC Power Distribution Architecture

MOHD TARIQ<sup>1,2</sup>, (Student Member, IEEE), ALI I. MASWOOD<sup>1</sup>, (Senior Member, IEEE),  
CHANDANA JAYAMPATHI GAJANAYAKE<sup>3</sup>, (Senior Member, IEEE), AND  
AMIT K. GUPTA<sup>1,2</sup>, (Senior Member, IEEE)

<sup>1</sup>School of Electrical and Electronic Engineering, Nanyang Technological University, Singapore 639798

<sup>2</sup>EPSIL@N, Rolls-Royce@NTU Corporate Lab, Nanyang Technological University, Singapore 639798

<sup>3</sup>Rolls-Royce Singapore Pte. Ltd, Singapore 638673

Corresponding author: Mohd Tariq (mohd0017@e.ntu.edu.sg)

This work was supported by the National Research Foundation Singapore under the Corp Lab@ University Scheme and was conducted within the Rolls-Royce@NTU Corporate Lab.

**ABSTRACT** With an aim to decrease pollution level due to aviation transportation sector, aircraft industries are focusing on more electric aircraft (MEA). The design of MEA is made with an aim to reduce the CO<sub>2</sub> emission, noise pollution, increased comfort level for the passengers, and so on. In this paper, a detailed study of the evolution of the MEA along with the load profile for electrical load is presented. Based on the requirements of the electrical load, a high-energy-density lithium-ion “Li iron phosphate” battery is selected, designed, and modeled. The modeling is based on the modified Shepherd curve-fitting model with the addition of the voltage polarization term to have a lower complexity and more proximity with the real battery profile. The phase shifted high power bidirectional dc–dc (PSHPBD) converter is used in the battery energy storage system (BESS) as a battery charger. The modeled Li-ion battery is integrated to the 270-V<sub>dc</sub> MEA power distribution bus using the optimal harmonic number-based harmonic model of the PSHPBD converter. Since BESS has to provide the transient loads, the fast dynamic response is required for the PSHPBD converter working as the charger in the BESS. A predicted peak current-based fast response control technique is proposed in this paper for the integration of the BESS with an MEA power system architecture. The proposed control structure provides a maximum limit on the coupled inductor current to the predicted peak current value as well as it gives fast transient response desired in the MEA system.

**INDEX TERMS** More electric aircraft, Li-ion battery, battery energy storage system, dc–dc converter, Shepherd model, harmonic model, peak predicted current control.

## I. INTRODUCTION

The global traffic in aviation sector is growing at the rate of approximately 7% in the last two years. This growth is in double digit in many developing countries like India [1]. With the growth rate as shown in Fig. 1, the contribution of aviation transportation in greenhouse gas emission is expected to increase. Therefore, for a sustainable environment, there is a need to develop a more sustainable and fuel efficient aircraft. The researchers and engineers have designed the more electric aircraft (MEA) in which the conventional system powered by the pneumatic and hydraulic sources are replaced

by the new systems powered by the electrical sources [2]. The MEA has been developed with an ultimate goal of distribution of electrical power across the airframe. More electrically powered aircraft has many advantages such as less maintenance, low weight, high reliability and passenger comfort. In the past years, many research has been done and many projects has been undertaken, which resulted in the deployment of large number electrical devices in large civil aircrafts by Airbus and Boeing [3]–[6]. Although, many research papers are available in the literature but none of them cover the evolution and load management of the MEA

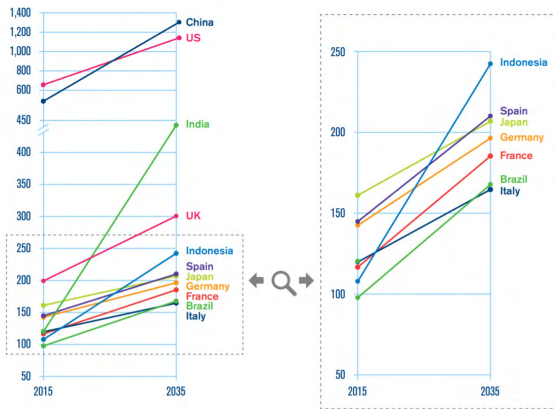


**FIGURE 1.** Growth projection of passengers in million during the year 2015-2035 [1].

with respect to the design of the energy sources. In this paper, a detail load profile of the MEA is presented so as to understand the requirements of the energy sources and the power converters.

The electrical power requirement in the MEA has grown tremendously and to support it, a high energy density battery energy storage system (BESS) is required. The power distribution architecture of the MEA is shown in Fig. 2. The BESS consists of a high energy density battery system and a phase shifted high power bidirectional dc-dc (PSHPBD) converter (as a battery charger). The BESS functionality includes the supply of the emergency loads besides the starting of the engine starter generator (ESG), thus making BESS as one of the very important part of the MEA. Therefore, the design of the best battery system along with its modeling holds an important role in the more electrification of an aircraft. In literature, many research are available on the design of battery system for other applications such as for electric vehicles (EVs), the nickel and the lithium based batteries have been widely used [7], [8], whereas in renewable energy applications valve regulated lead acid battery [9], lithium ion battery [10], sodium sulphur (NaS) battery [11], etc. are used. However, in literature, there is a gap on the best design and modeling of BESS for MEA, hence in this paper an approach

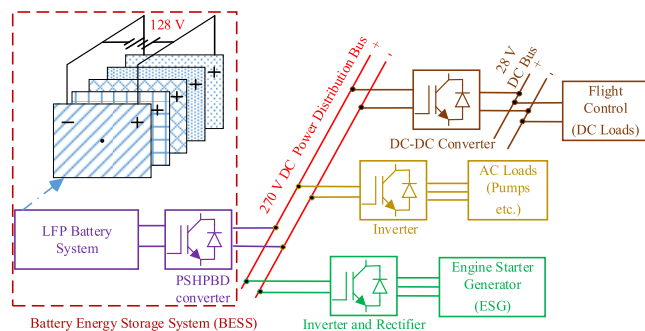


**FIGURE 2.** The proposed integration of battery energy storage system (BESS) to 270 V DC power distribution architecture in MEA.

is devised based on the electrical loading profile for the designing of the best BESS in MEA. As already stated that the BESS has two components, battery and PSHPBD converter, hence a modeling approach for both have to be defined and carried out. In literature, the battery modeling is classified into three categories: the equivalent circuit modeling of the battery using voltage sources, capacitors and resistors forming a circuit network [12], the modeling of the battery based on neural network [13], and the modeling of the battery based on the simplified electrochemical model [14]. In [15], advanced sparse Bayesian predictive modeling methodology was employed to monitor state of health (SOH) and remaining useful life was forecasted. Whereas in [16], the fast charging strategy is formulated as a linear-time-varying model predictive control problem. In [17], a thermal model for a cylindrical Li-ion battery based on the finite element method is presented and discussed wherein the battery temperature distribution is simulated. In the electrochemical based modeling approach, Shepherd model is mostly used for the analysis of the battery in electric vehicle applications. In [18], a fractional-order circuit model is adopted to predict battery dynamic behaviors and a general algorithm was applied to estimate lithium-ion battery states. It is reported in literature that generally, high-fidelity models have high modelling accuracy but it also has a very heavy computation [19], thus for a complex system like MEA, modified Shepherd-curve-fitting model is used for the modeling of the Li-ion battery.

Moreover, to understand the system level operation of the power system architecture in MEA, it is imperative to deal with the mathematical model of the components. The motivation of the present work is to develop a system level simulation capability for the MEA system, for which a low complex modeling of the Li-ion battery is reported in this paper. Furthermore, for the system level interaction of the PSHPBD converter and its controller design an optimal harmonic number based modeling is reported here. The optimal harmonic number is the Fourier series equation based modeling which does not include small integration time steps thus making it possible to compute it effectively.

In literature, the PSHPBD converter is modeled using the modeling for rms and average currents [20] and the generalized average modeling approach [21]. But the modeling of the PSHPBD converter based on the comparison of power transfer between analytical model and the Fourier series based harmonic model for the power rating of the MEA system is missing in the literature.

After the design and modeling of the BESS, the next uphill task is to effectively integrate the BESS with the MEA power system architecture. With the integration of the BESS to the main distribution network, a power management strategy can be implemented wherein the electrical generators will supply the load and the BESS will take care of the transient etc. The aforementioned strategy of power management is having a huge potential benefit as it will save the electrical generator from taking extra loads and thus will be efficient in longer run. Since, the BESS has to provide the transient

loads, the traditional control strategy like single phase shift control [22] and advanced control strategies like dual phase shift control [23], triple phase shift control [24] and extended phase shift control [25] may not be able to provide the required transient response in one switching cycle as all these controls have either single or double loop control structure involving the PI regulator. These advanced control techniques also require two or more degree of freedom (variables) and thus are not suitable for the MEA applications as solution of multi variables make the system complex for execution. Moreover, these control techniques may also make the transformers saturate on steeply changing the transformer current for large scale change in the load. Thus, in the presented work, a fast response control technique is proposed which effectively integrates the BESS to the MEA power distribution network. Moreover, the data, design and modeling presented in this paper are for the real parameters of an MEA, hence the presented work will help the engineers/researchers working in the field of the BESS and its integration to the MEA power system architecture to understand the system in a better way.

The rest part of the paper is structured as follows: Section II details the evolution of the MEA, Section III details the design and modeling of the lithium ion battery system. The design and modeling of the PSHPBD converter is presented in section IV. BESS integration to the MEA power system architecture is discussed in section V in which predictive current control technique is given in detail. Section VI concludes the paper.

## II. EVOLUTION OF MORE ELECTRIC AIRCRAFT

With the advancement in the area of electro-mechanical actuators, electro-hydrostatic actuators, fault-tolerant electrical power systems, fault-tolerant electric machines and power electronic systems and their use in MEA has resulted in it gaining tremendous benefits over its conventional counterpart. The following benefits are reported in literature for the MEA in comparison to the conventional aircraft [26], [27].

- **Reduction in the complexity of the aircraft system with the replacement of the engine-bleed system by electric motor-driven pumps.** It also reduces the installation cost.
- An increased reliability in the aircraft with the removal of the hydraulic systems. It will also reduce the complexity of the system beside reducing the weight, installation and running cost.
- **The accessory gearboxes, power take-off shaft and the engine tower shaft and gears has been eliminated with the use of engine starter/generator (electrical power) in starting for the aero-engine.** This has reduced the starting power required for starting engine especially in the cold condition.

Moreover, in MEA, the use of bleed air has been eliminated for environmental control system (ECS). In conventional aircraft, the cabin pressure and temperature were regulated by ECSs by tapping bleed air for achieving passenger comfort. Bleed air were tapped from one of the compressor stages of the main engine. But in MEA like Boeing 787, a set of

compressors are used for regulating the pressure and temperature in the cabin. This has resulted in the elimination of the air ducts and pneumatic system from the engine. Since a large amount of power is required for regulating the cabin pressure and temperature, hence main generators power generation capacity has to be increased. Beside this, electrical power is also used to start the main engine in the MEA. The pneumatic systems is further eliminated by the electric start of the main engine in the MEA. The above cases are the examples of the transitioning to pure electric systems from various other systems in the MEA. In short, the aerospace industry has been revolutionized with the adoption of the MEA as it has significantly improved the industry with respect to fuel consumption, aircraft-empty weight, overall cost system reliability, reconfigure ability, supportability and maintainability.

With the aforementioned benefits of the MEA, in the first decade of the 21th century engineers worked on the deployment of the MEA in the civil aviation sector. As seen in Fig. 3 the aircraft main generator power capacity is increased to 1 MW level for Boeing-787. Fig. 4 shows the ratio of electrical power per passenger capacity ratio of the civil aircraft in the last 5 decades. For the conventional aircraft, this ratio is around 1-1.5 kW/passenger, whereas for the case of an MEA, this ratio is 3 kW/passenger. Airbus A380 and A350, both have high electrical power requirement as seen in Fig 3, but this high requirement is due to the fact that the number of passengers in both the aircraft are higher. The work presented in this paper details the profile and parameters of Aircraft "X" which is proposed to be the more electric version of the aircraft of the capacity of Boeing 717. Table 1, details seating capacity and distance range details of the civil aircrafts named Boeing 787, Airbus 380, Airbus 350, Boeing 767, Boeing 717 and Aircraft "X". Since for the service within the country or within the continent (i.e. interstate/intercity) requires smaller aircraft, Aircraft "X" is designed for 100 passengers

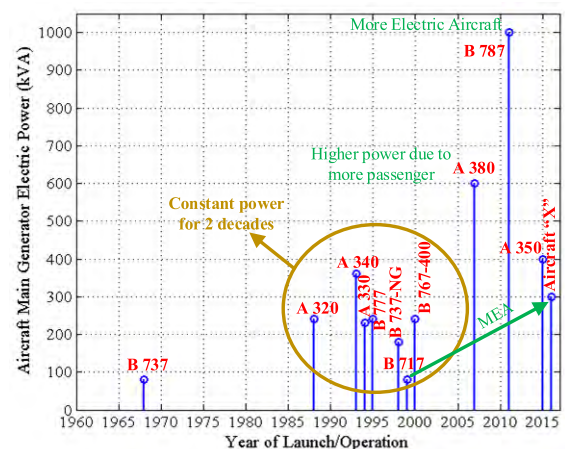


**FIGURE 3.** Power growth in the major civil aircraft (Airbus and Boeing) during 1965 -2015.

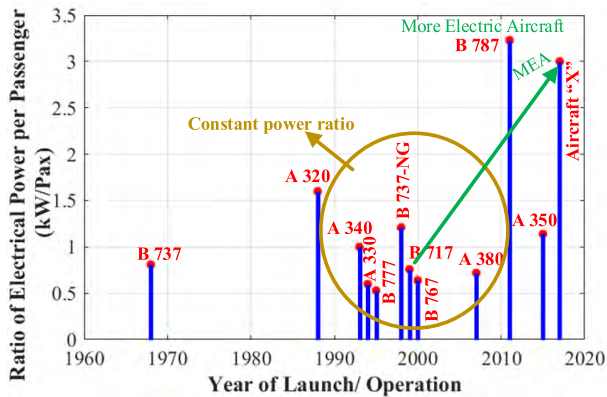


**FIGURE 4.** Electrical power per passenger ratio in the major civil aircraft (Airbus and Boeing) during 1965 -2015.

**TABLE 1.** Seating Capacity And Distance Range details of the civil aircrafts.

Aircraft	APU/Generator power	Seats	Flight range
Boeing 787	450 kVA	242 - 335	15,190 km
Airbus 380	120 kVA	525 - 853	15,700 km
Airbus 350	150 kVA	280-366	15,100 km
Boeing 767	120 kVA	245	10,418 km
Boeing 717	60 kVA	117	3,815 km
Aircraft "X"	50 kVA	100	5,000 km

capacity with a flight distance range of 5000 km (interstate for bigger countries like USA, India, China, Russia etc.).

#### A. ELECTRICAL LOAD PROFILE OF THE MEA

In this section, the electrical load profile of the Aircraft "X" is given in detail so as to understand the requirement of the BESS for the best design criteria. The rating of the auxiliary power unit (APU)/ESG is 50 kVA in the Aircraft "X", while the main generator capacity has the power rating of 100 kVA. Since, Aircraft "X" uses two engine generators and two main generators, hence the total electrical power rating equals 300 kVA for 100 passengers' aircraft. This makes the electrical power per passenger ratio to be 3, which qualifies it to be an MEA.

#### 1) ELECTRO-MECHANICAL ACTUATORS (EMA)

In an MEA, there are a number of conventional pneumatic and hydraulic based actuators which are replaced by the electro-mechanical (EMA) actuators. The electrical power rating and profile of some of the actuators used for operating aileron, spoiler and rudder are given in this section. EMA generally consists of a high speed electrical machine which is coupled to the mechanical load (gearbox connected to the roller screw or ball).

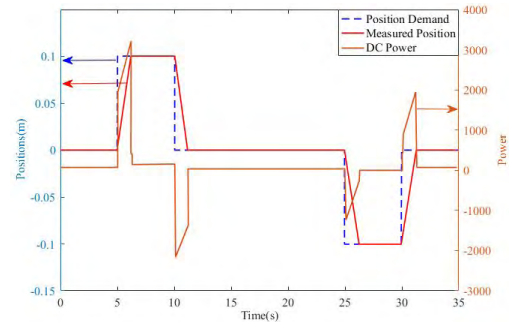


**FIGURE 5.** DC power requirement for Ailerons operated by the EMA.

#### a: AILERON OPERATED BY EMA

The dc power requirement of the EMA with respect to the change in position of aileron is shown in Fig. 5. Depending upon the movement of the surface, the aileron EMA consumes as well as regenerates the electrical power (if regenerative drives are used [28]). If the surface moves in opposite direction to the force applied, aileron EMA will consume electrical power. Whereas, if the surface moves in the direction of the force applied, aileron EMA will regenerate electrical power. As seen in Fig. 5, for time  $t = 0$  seconds to 5 seconds, aileron requires a constant 90 W of electrical power also known as "holding power". At time  $t = 5$  seconds, the aileron is moved by EMA and the aileron surface position is changed from 0 m to 0.1 m. As the aileron is operated by EMA, hence for the change in position, 3 kW of electrical power is required. After the position is changed from 0 m to 0.1 m (during time  $t = 5$  to 7.42 seconds), the motor speed will become zero and hence the EMA will not require extra power. But for holding the aileron surface at 0.1 m (during time  $t = 7.42$  to 10 seconds), a holding power of 240 W is required. This whole change will occur in 2.42 seconds thus creating a transient disturbance on the power distribution network of the MEA. In the proposed strategy of BESS assisted electrical generator system, BESS can support the additional transient loads due to the operation of aileron EMA whereas generator can be loaded for holding power requirement of the aileron EMA. At time  $t = 10$  seconds, the position is decreased from 0 m to -0.1 m, thus regenerating the electrical power of 2 kW which can be used for charging the BESS. Similarly, for lower change in position, low dc power will be required by the EMA as shown during time  $t = 25$  to 32.42 seconds. Thus, from fig. 5 it can be concluded that the transient electrical power requirement of an aileron operated by the EMA is 3 kW.

#### b: SPOILER OPERATED BY EMA

In aero-plane, spoilers are used for intentionally reducing the lift component in a controlled way. They are mostly used during the descent and landing phase of the journey. In the MEA, the spoilers are operated by the EMA. Fig. 6 shows the dc power requirement by the EMA for operating spoilers in two different cases. For the extension angle



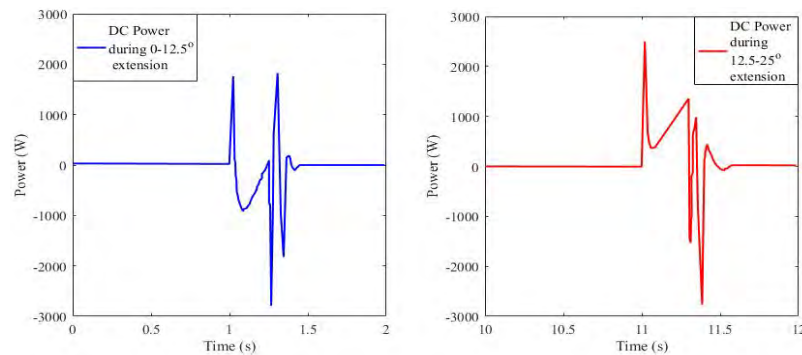


FIGURE 6. DC power requirement for Spoilers operated by the EMA.

of  $0^\circ - 12.5^\circ$ , the peak dc power required is 1.7 kW whereas for the extension angle of  $12.5^\circ - 25^\circ$ , the peak dc power required is 2.5 kW. Moreover, during landing, spoilers are fully deployed (opened by maximum angle of extension) to slow down the plane, thus requiring peak power to the level of 3- 4 kW. As seen from Fig. 6, the electrical profile of the spoiler is highly non-linear in nature which will have a deteriorating effect on the electrical generator system. Thus, in the proposed strategy of BESS assisted electrical generator system, BESS can support the additional transient loads due to the operation of spoiler EMA.

#### c: RUDDER OPERATED BY EMA

The rudder is used in the aircraft to change the horizontal direction of the plane. Ailerons and rudders are used in conjunction, producing coordinated turns to change the direction of the plane. In the MEA, the rudders are operated by the EMA. Fig. 7 shows the electrical load profile of the EMA required for operating the rudders. When the rudders are opened, it requires a transient electrical power of 3.2 kW for the duration of 2 seconds (in Fig. 7, during time  $t = 5$  to 7 seconds and  $t = 25$  to 27 seconds). Whereas, when the rudder is closed, it can regenerate electrical power if EMA is operated by the regenerative drive. The regenerated power shown in Fig. 7 is 2.2 kW. Again, in the proposed strategy

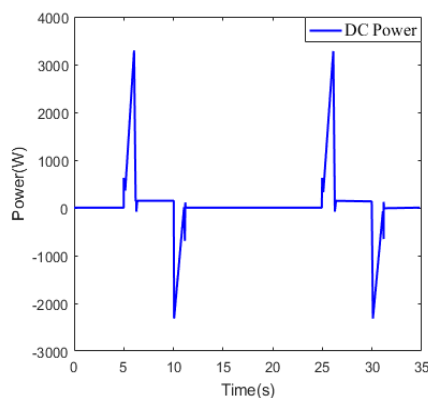


FIGURE 7. DC power requirement for Rudders operated by the EMA.

of BESS assisted electrical generator system, BESS can support the additional transient loads due to the operation of spoiler EMA.

Thus, it can be concluded that for the operation of the EMA in the MEA, the proposed strategy of BESS assisted electrical generator system is necessary so as to share the transient/dynamic power and the steady state power accordingly. The proposed power sharing strategy will improve the power quality and reduce the impact of the transient electrical loads on the generator.

#### 2) ENGINE STARTER GENERATOR (ESG) STARTING PROFILE

With an objective of saving weight and space and to attain a higher efficiency in the MEA system, the MEA are equipped with the engine starter generator systems. ESG systems contain an additional winding which allows it to function as a generator once the engine has attained a self-sustaining speed. MacMinn and Jones have used a high speed switched-reluctance motor (SRM) for starter generator applications. Fig. 8 shows the starting profile (electromagnetic torque and speed characteristics) of the ESG for the proposed Aircraft “X”. Different modes of control i.e. speed control, torque control and voltage bus control modes for the ESG are also shown in the figure. Fig. 8 shows that the starting time

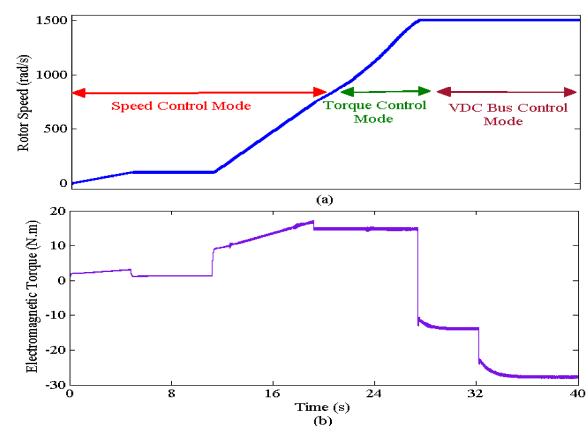


FIGURE 8. ESG starting profile of the MEA.

required for the ESG is 27 seconds, the condition when the electromagnetic torque become negative from the positive. The starting power calculated from the figure is 22.5 kW and since the Aircraft “X” is a twin engine aircraft hence the total power required from the BESS for starting is 45 kW. In Aircraft “X”, provision is made to start the ESG by the BESS, hence considering losses in the conductor, power electronic converters etc., the BESS has to be designed for a power rating support of 50 kW. As a matter of safety and following the recommendations given in the literature, the starting time is taken for the worst-case scenario (three attempts to be made for starting). The starting time is taken as 5 minutes in general. Hence the min. energy required by the BESS will be  $(\{50/60\} \times 5 = 4.17 \text{ kWh})$ .

### 3) TRANSIENTS ON 270 V DC BUS

The MIL-STD-704F standards (commonly known as military standard) was released on 12 March 2004 with a purpose to ensure compatibility between the external power system, aircraft electric system and airborne utilization equipment [32]. The military standard (MIL-STD-704F) is for establishing the electrical power requirements at the input terminals of the equipment in the MEA utilizing electrical energy. MIL-STD-704F standardize the transient profile of the 270 V DC bus of the MEA Aircraft “X”, which is shown in Fig. 9. As shown in Fig. 9, there is a 30 V steady-state voltage allowance (250 V-280V). In the case of voltage going below 250 V, it has to be boost up to the level of 250 V within the time limit of 30 milliseconds. Furthermore, if somehow the voltage on the 270 V DC bus exceeds the 280 V limit, then it has to be step down to the level of 280 V within the time limit of 20 milliseconds. This boosting up (by injecting extra power) and step down (by regeneration of power) can be achieved by the BESS employed in the MEA as the power injection and regeneration can be easily supported by the BESS.

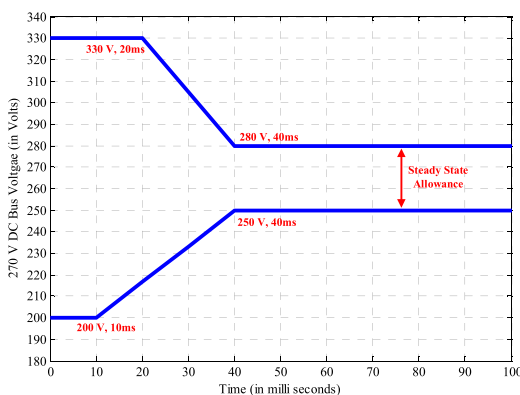
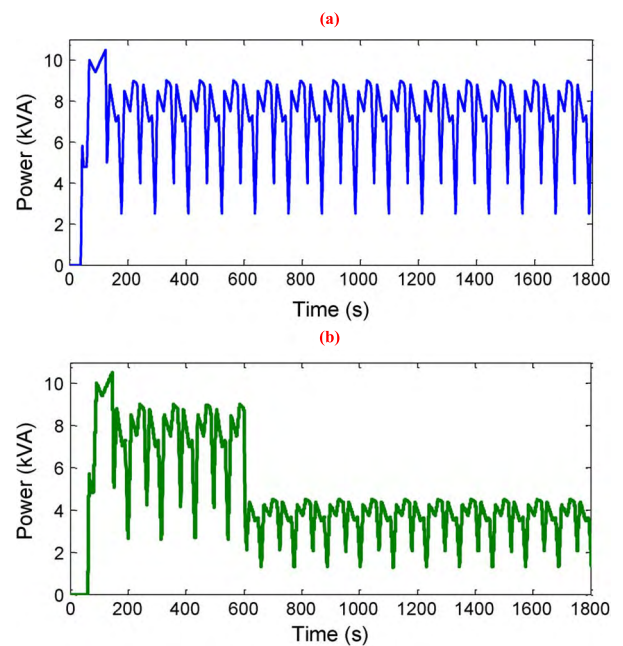


FIGURE 9. MIL Standard for 270 V DC bus architecture.

### 4) EMERGENCY LOAD PROFILE

There are many avionic loads which need to be operated by electrical power after the incorporation of the EMA in the

MEA during the emergency period. The electrical loads such as the operation of the flaps, ailerons, rudder, landing gear etc. is necessary for the safe landing of the plane in case of engine and generator failure. There are various control/display board loads operated on 28 V DC bus which need to be supplied with electrical power in the case of emergency. Fig. 10 shows a typical load profile during the emergency operation for Aircraft “X”. Federal Aviation Administration (FAA) recommends the emergency loading for 30 minutes [29]. As seen in Fig. 10, 10 kVA of electrical load is shown for 30 minutes in the first case whereas in the second case 10 kVA of electrical load is shown for the first 10 minutes and 5kVA of load for the remaining 20 minutes. In case of engine/generator failure, this electrical power has to be supplied by the proposed BESS in the MEA Aircraft “X”.



Load profiles of a 30-min emergency landing scenario

FIGURE 10. Emergency Load Profile (a) 100 % loading case (b) 50 % loading case [29].

## III. LITHIUM ION BATTERY SYSTEM FOR MEA

In section II A, the details of the electrical load profile of the MEA is explained. It is noted that with the implementation of the EMA in the MEA, there is an increase in the number of transient loads on the power distribution DC bus. To supply the electrical loads discussed in the above section during the transient periods it is imperative to design and model the battery system in an effective way. For electric vehicle application, lithium ion batteries are state of the art because it offers high energy density [31]. But for the MEA application the lithium ion batteries are neither explored much in research nor in practice. Boeing 787 and Airbus 350 have used lithium ion battery in the civil segment.

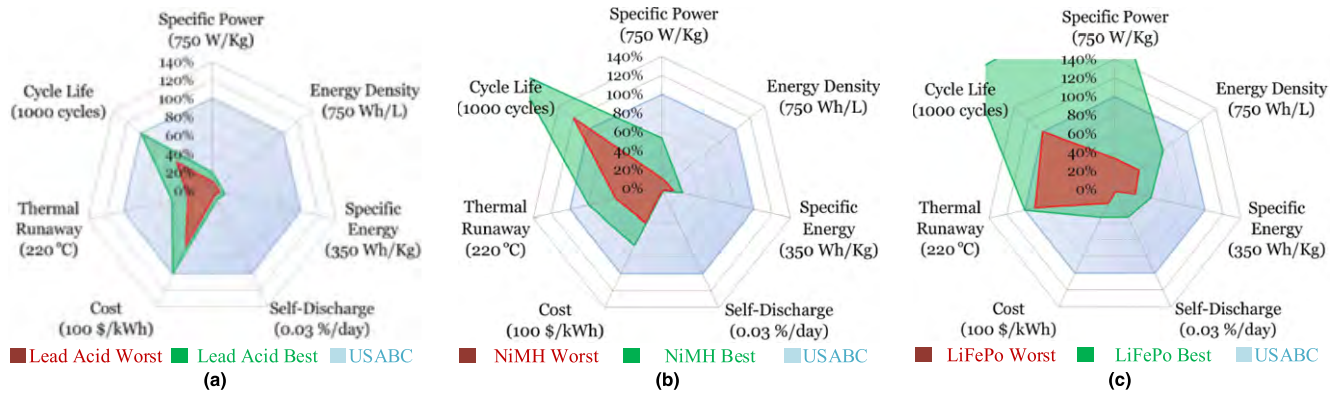


**FIGURE 11.** Spider web diagram showing specific power, energy density, self-discharge, cost, thermal runaway and cycle life of (a) Lead Acid (b) Nickel Metal Hydride (c) Lithium Ferrous Phosphate battery technologies [31].

### A. DESIGN AND CONNECTION

In the MEA, safety/reliability and lightweight are the critical factors in designing any components. The high energy density and small size (with high reliability and safe operating behavior) battery system is recommended for implementation in the MEA as in [33] and [34], it is reported that 1700 and 5400 tons of saving per year in fuel and CO<sub>2</sub> emission respectively is achieved for all air traffic worldwide with 1 kg decrease in the weight of the component in the aircraft. Moreover, with reduced component weight, the chance of increasing the payload is higher and it is also reported in [35] and [36] that with 1 kg decrease in the component weight of the aircraft, there would be an approximate saving of 1000 US \$ in lifetime fuel burn cost.

In this section, the design of the battery system is done considering the following requirements of aircraft grade batteries:

- It should be safe (not prone to thermal breakdown)
- It should deliver power continuously irrespective of the operating environment.
- It should be light in weight.
- It should be able to supply power for long time (long life).

Figs. 11 (a), (b) and (c) show the spider web diagram of the a) Lead Acid (b) Nickel Metal Hydride (c) Lithium Ferrous Phosphate battery technologies respectively wherein specific power, energy density, self-discharge, cost, thermal runaway and cycle life are plotted on a spider web [31]. The United States Advanced battery Consortium (USABC) has specified certain goals shown in Fig. 11 for the year 2020. It is observed from the spider web that lithium ferrous phosphate “LiFePO<sub>4</sub>” (LFP) battery technologies is covering maximum area in the spider web diagram. Moreover, LFP battery chemistry has a higher discharge current handling capability (up to 35 C A discharge current). This motivates to select the LFP battery system in the proposed BESS installation in the MEA Aircraft “X”. The design (rating) of the LFP battery system is based on the rating of different electrical loads for

the battery system given in Table 2.

$$\text{State of energy (SOE)} = \left[ 1 - \frac{\text{Energy Required}}{\text{Battery Energy}} \right] * 100\% \quad (1)$$

$$\text{Depth of charge (DOD)} = 100\% - \text{SOE} \quad (2)$$

$$\text{Output Current of Battery} = \frac{\text{Power Required}}{V_{\text{battery}}} \quad (3)$$

Fig. 12 shows the proposed connection of the LFP battery system, wherein 5 LFP batteries are connected in series to achieve 128 V. One LFP battery for aircraft grade has the rating of 25.6 V with 45-55 Ah capacity [37]. Thus, one LFP battery is capable of delivering 1280 Watt for 1 hour ( $50 \times 25.60 = 1280$  Watt-hour). The proposed connection shown in Fig. 12 can deliver 6400 watt-hour. 50 kW is required for the starting of the ESG and in the worst condition time taken for starting is 5 minutes. The proposed connection of the battery system can deliver 50 kW of power for 5 minutes for starting the ESG. From eqn. (1), SOE after the start of the ESG is 34.90 % and DOD from eqn. (2) is 65.10 %. The SOE of 34.90 % is deemed to be acceptable level after the start of the ESG, as there might be some transient loads which needs to be powered up by the BESS immediately after the ESG starting. Eqn. (3) gives the current required from the battery, which is equal to 390.63 A. The desired current can be achieved with 8 C discharging rate which is feasible as can be seen from Fig. 13. Fig. 13 shows the nominal voltage achieved is between 100 V to 140 V. This voltage variation of the battery can be corrected by the DC-DC converter (working as a battery charger). Thus, a 6.4 k Watt-hour, 50 k Watt battery system is designed for the MEA Aircraft “X”.

### B. MODELING OF LI-ION BATTERY SYSTEM

Aircraft power system architecture has battery systems, multiple dc-dc converters, multiple dc-ac inverters and similarly many ac-dc rectifiers besides having different electrical machine as loads. System level studies are important to understand the behavior of one system in the presence of other

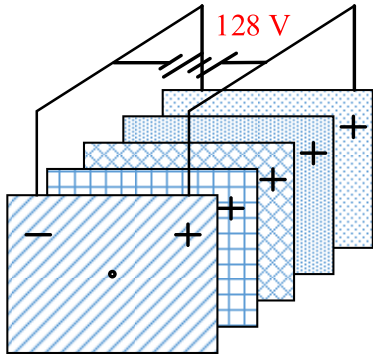


FIGURE 12. Five Lithium Ion battery connected in series.

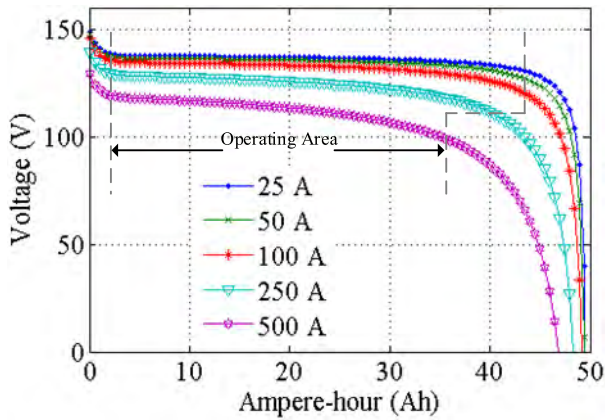


FIGURE 13. Voltage-Ah characteristics of the LFP battery at different C rate.

TABLE 2. Electrical load for battery system.

Electrical Battery System	Load for	Power (in kW)	Time (in seconds)	Energy (in kWh)
Engine Starter Generator		50	100	1.389
Emergency Load		10	1800	5.000
Aileron	3 * 6 = 18	2.2		0.011
Spoiler	4 * 4 = 16	0.5		0.002
Rudder	3 * 2 = 6	2		0.003

systems. For system level interaction, it is necessary to have modeling based approach so as to avoid the complexities. In this section, the lithium ion battery is modeled. In the electrochemical based modeling approach, Shepherd model is mostly used for the analysis of the battery in electric vehicle applications. The Shepherd model describes the electrochemical behavior of the battery system (lithium ion battery in the presented application) in terms of current and voltage. The battery model in Sim Power system (SPS) in MATLAB<sup>®</sup> is based on the shepherd model [38]. In this work, modified Shepherd-curve-fitting model is used. The modeling of the battery is shown in Fig. 14, wherein the voltage polarization

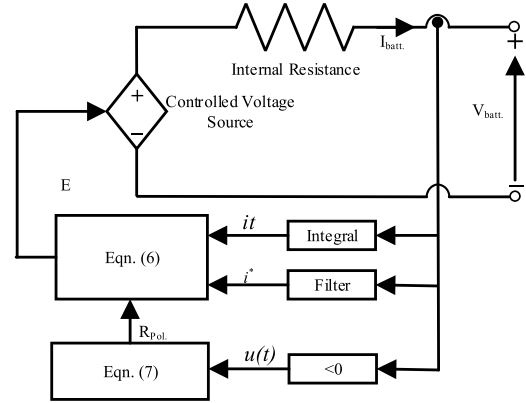


FIGURE 14. A Li-ion battery model (includes the additional polarization term).

term is added in the expression of the battery discharge voltage. With the addition of the voltage polarization term, the effect of the battery SOC can be expressed in a better way on the battery performance. Moreover, in this work a filtered battery current is also used so as to determine the rate of discharge which accounts for the polarization resistance. The equation used in the modeling are given in eqns. (4) to (7).

$$V_{batt} = E_o - K \frac{Q}{Q - it} \cdot it - R_b \cdot I - A_b \cdot \exp(-B \cdot it) - K \frac{Q}{Q - it} \cdot i^* \quad (4)$$

$$R_{Pol.} = K \frac{Q}{it - 0.1Q} \quad (5)$$

$$E = E_o - K \frac{Q}{Q - it} \cdot it + A_b \cdot \exp(-B \cdot it) - R_{Pol.} \cdot i^* \quad (6)$$

$$R_{Pol.} = K \frac{Q}{Q - it} (1 - u(t)) + K \frac{Q}{it - 0.1Q} u(t) \quad (7)$$

Where  $K$  = constant of polarization (volts/Ah),  $E_o$  = constant battery voltage (in V),  $i^*$  represents the filtered battery current (A),  $A_b$  = amplitude of the exponential zone (V),  $B$  = inverse of the exponential zone time constant ( $\text{Ah}^{-1}$ ), and  $R_b$  = internal resistance of the battery (in ohms).  $Q$  is maximum battery capacity in (ampere-hour) whereas “ $it$ ” is the actual battery charge (in ampere-hours).

Eqn. (4) gives the battery voltage whereas eqn. (5) gives the polarization resistance. During the process of charging, once the battery becomes fully charged, the battery voltage increases abruptly. This real-time behavior of the battery is represented in the model by eqn. (5), which modifies the polarization resistance. The battery system is modeled in the SPS block set of the MATLAB<sup>®</sup> using Fig. 14 and is compared with the existing standard model in MATLAB<sup>®</sup>. The comparison results are captured and presented in the Figs. 15 (a) – (d), wherein a close match has been observed between the two models.



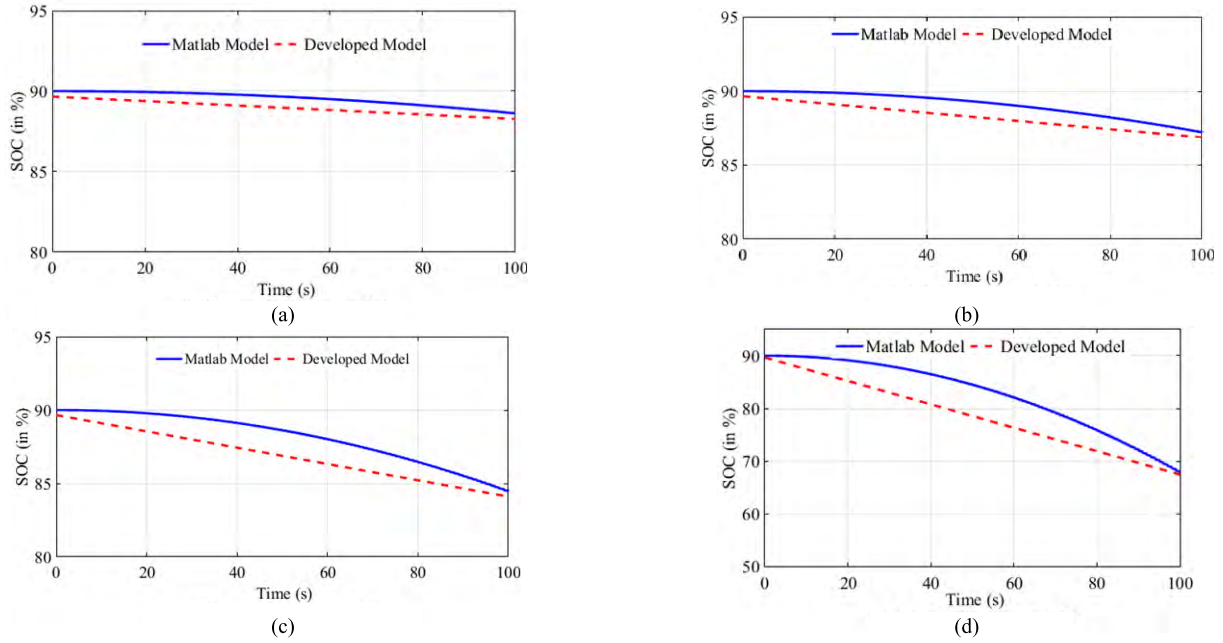


**FIGURE 15.** Comparison of MATLAB® Battery model and developed battery model: (a) At 0.5 C discharge rate. (b) At 1 C discharge rate. (c) At 2 C discharge rate. (d) At 8C discharge rate.

#### IV. BATTERY CHARGER CIRCUIT [PHASE SHIFTED HIGH POWER BIDIRECTIONAL DC-DC CONVERTER]

A full bridge bi-directional isolated DC-DC converter is required for the integration of the battery system with the main power distribution architecture of the MEA Aircraft “X”. The bi-directional flow of power is required owing to the requirement of the charging and discharging of the battery with the same converter, which will reduce the size and weight of the system. An isolated converter is required in order to isolate the battery system in case of any fault in the main distribution network of the MEA Aircraft “X”. As shown in Fig. 2, BESS is integrated to the main power distribution 270 V DC bus using a phase shifted high power bi-directional DC-DC (PSHPBD) converter. PSHPBD converter shown in Fig. 16 (a) is the preferred topology for the BESS as it offers a bidirectional, isolated, high power

$$G = \frac{v_o}{nv_i} \quad \text{and} \quad G = \frac{270}{2 * 128} = 1.06 \quad (8)$$

density and efficient power conversion. The PSHPBD topology originally proposed and published in 1991 by De Doncker *et al.* [39], has been extensively used in the electric vehicle applications including for the MEA for battery system integration. As stated earlier, the MEA Aircraft “X” power system architecture has many components hence for an effective simulation based system level interaction studies will require an effective and less complex modeling of each component. In this section, first the PSHPBD converter is designed with respect to the parameters and requirements of the MEA Aircraft “X” and then it is modeled for performing system level interaction with other components.

#### A. DESIGN OF PSHPBD CONVERTER

The maximum power transfer, output and input voltages are the main specifications deciding the characteristics of the PSHPB DC-DC converter. The requirement of the volumetric size of the PSHPBD converter decides the value of the switching frequency. Fig. 16 (a) shows the schematic of the PSHPBD converter whereas the key operating waveforms of the said converter is shown in Fig. 16 (b). The transformer turn ratio (1:n) is designed in order to achieve G (ratio of output referred voltage to the battery voltage) equal to 1. In this work, G is calculated to be 1.06 from eqn. (8).

The duty cycle ( $d$ ) and coupling inductor ( $L_s$ ) design is presented in this section. The design of the ( $d$ ) and ( $L_s$ ) is done keeping in mind the following things:

- Flow of maximum power between the primary and secondary bridges of the converter.
- ZVS operation of the converter in wide range of load.

Fig. 16 (b) shows the inductor current ( $i_L$ ) waveform wherein lossless component and piecewise linear waveform has been assumed for deriving necessary eqns. In the inductor current

$$I_{pk} = [V_o(2d - 1) + nV_{in}] \frac{T_s}{4L_s} \quad (9)$$

$$I_r = [nV_{in}(2d - 1) + V_o] \frac{T_s}{4L_s} \quad (10)$$

$$P_{transfer} = \frac{nV_{in}V_o(d - d^2)}{2L_sF_s}; \quad P_{norm.} = (d - d^2) \quad (11)$$

$$L_s = \frac{nV_{in}(d - d^2)}{2I_oF_s} \quad (12)$$

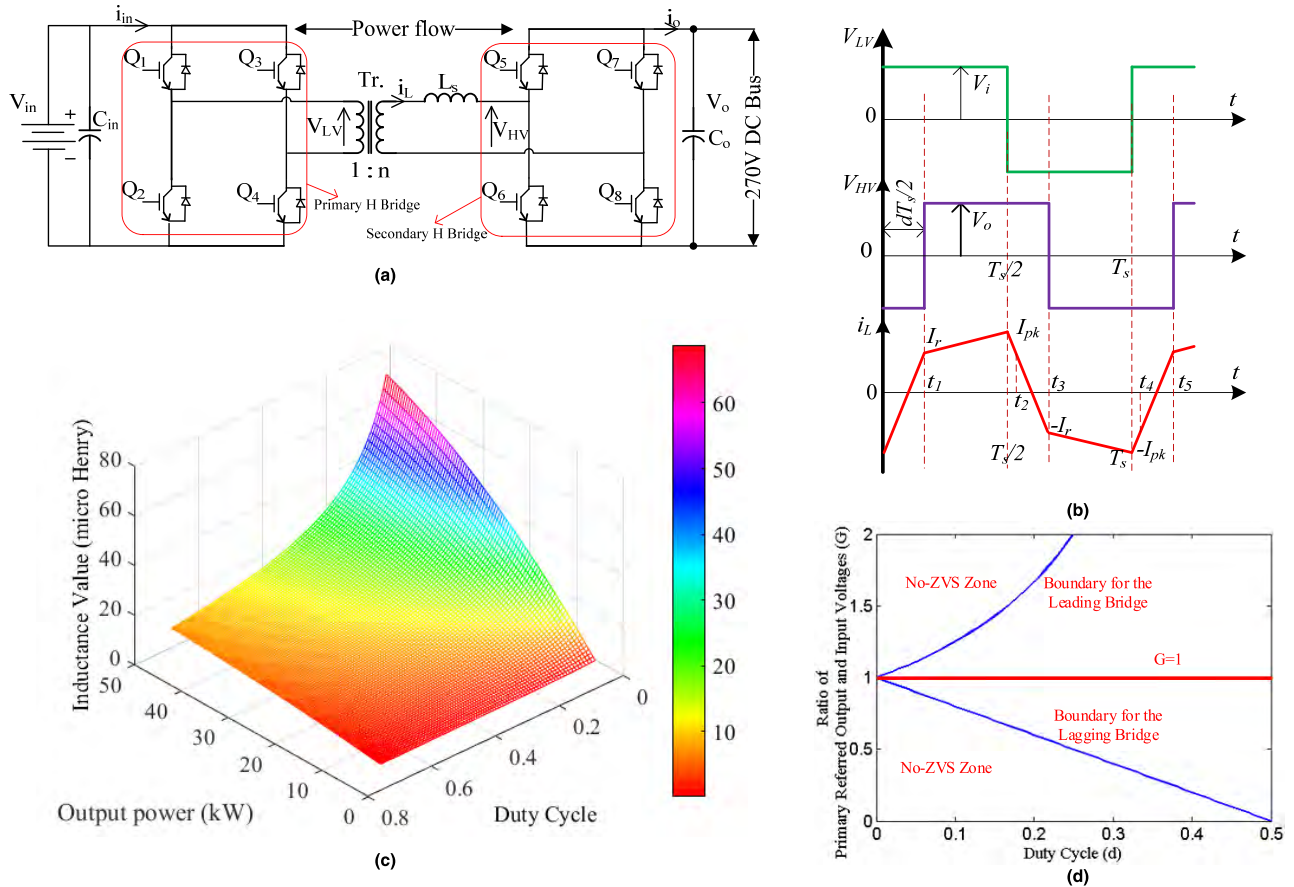


**FIGURE 16.** (a) Schematic of PSHPBD converter. (b) Key operating waveforms of PSHPBDC. (c) Output power and duty cycle effect on the coupling inductance. (d) Boundary condition for No-ZVS zone.

waveform, two positions are marked i.e instant for switching of the primary and secondary bridges are given in eqns. (9) and (10) respectively.

Solving eqns. (9) and (10) gives the total power transfer which is represented mathematically in eqn. (11). Eqn. (11) also gives the normalized power transfer, which helps to design the value of “ $d$ ” for maximum power transfer. The “ $d$ ” is taken as 0.5 for maximum power transfer. A relation between the inductance value of the coupling inductor ( $L_s$ ) and duty cycle ( $d$ ) is shown in Fig. 16 (c) in pictorial form. Fig. 16 (c) shows the dependence of coupling inductance ( $L_s$ ) on the “duty cycle,  $d$ ” and “output power,  $P_o$ ”.

The PSHPBD converter switching devices operates in ZVS mode for a particular load region as seen in Fig. 16 (d). The figure shows that for  $G = 1$ , there will be ZVS operation of the converter for the large variation in load. While integrating the battery system with the power distribution network using the PSHPBD converter, the value of  $G$  will change depending upon the SOC of the battery. Therefore, this effect has to be taken into consideration while designing an effective PSHPBD converter. The modified expression for the inductor current waveform is given in the eqns. (13) to (15). The eqns. (9) and (10) are modified by following the condition of ZVS that  $I_{pk}$  and  $I_r$ , both must be positive to

achieve ZVS.

$$I_{pk} = [2Gd + 1 - G] \frac{T_s v_{in}}{4L_s} \quad (13)$$

$$I_r = [2d - 1 + G] \frac{T_s v_{in}}{4L_s} \quad (14)$$

$$\text{For } G = 1; \quad I_{pk} = [d] \frac{T_s v_{in}}{2L_s} \text{ and } I_r = [d] \frac{T_s v_{in}}{2L_s} \quad (15)$$

$$d > \frac{1-G}{2} \text{ for } G < 1 \text{ and } d > \frac{G-1}{2G} \text{ for } G > 1 \quad (16)$$

From eqn. (15), it is clear that if the ratio ( $G$ ) is kept at 1, then  $I_{pk}$  and  $I_r$  will always be positive and hence ZVS will be achieved for all the values of “ $d$ ”. But when the ratio ( $G$ ) is not equal to 1 as in the presented work,  $G = 1.06$  for 100 % SOC and  $G = 1.35$  at 35 % SOC, then the calculation of “ $d$ ” is given by eqn. (16). Fig. 16 (d) is the pictorial representation of the eqn. (16). As seen in Fig 16 (d), that if “ $d$ ” is taken as 0.5, then from eqns. (11) and (16), maximum power transfer will be ensured along with ZVS for wider range of load.

$$E_{L_s} > E_{C_{par.}} \rightarrow \frac{1}{2} L_s i_{L_s}^2 > 4 \cdot \frac{1}{2} C_{par. (Eqv.)} V^2 \quad (17)$$

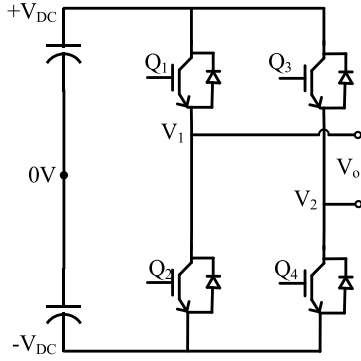


FIGURE 17. Primary Side of the PSHPBD (H- Bridge Converter).

TABLE 3. H- bridge truth table.

$Q_1$	$Q_3$	$V_1$	$V_2$	$V_o$
0	0	$-V_{DC}$	$-V_{DC}$	0
0	1	$-V_{DC}$	$+V_{DC}$	$-2V_{DC}$
1	0	$+V_{DC}$	$-V_{DC}$	$+2V_{DC}$
1	1	$+V_{DC}$	$+V_{DC}$	0

The coupling inductor value ( $L_s$ ) is designed from eqns. (12) and (17), as eqn. (17) gives the condition for the stored energy in the output capacitance (parasitic) “ $E_{Cpar.}$ ” and the coupling inductance ( $E_{Ls}$ ). Hence, for the presented case of MEA Aircraft “X”, the duty cycle “ $d$ ” is selected as 0.5 and  $L_s$  is selected as 8.64 micro henry.

### B. OPTIMAL HARMONIC NUMBER BASED MODELING OF PSHPBD CONVERTER

The modeling of the PSHPBD converter is necessary in the modeling of the BESS. For studying the system level behavior and interactions, simulations are required to be done. If PSHPBD converter is simulated with detailed model i.e. using the IGBTs switches available in the SPS block set of the MATLAB<sup>®</sup>, the simulation will be slow and it will be difficult to analyze the behavior of the BESS. Moreover, an accurate dynamic model is also required for obtaining the optimized/maximized performance and for the design of an effective closed loop control. Hence, in this section Fourier series based harmonic modeling of the PSHPBD converter is presented.

The building block of the Fourier series based harmonic modeling can be explained from Fig. 17 and table 3. Fig. 17 shows the primary side of the PSHPBD converter from which the values  $V_1$ ,  $V_2$ , and  $V_o$  can be calculated. The truth table 3 can be expressed mathematically as given in eqn. (18). Eqn. (19) defines the time domain expression for the switching states of each phase leg of the bridge.

$$V_o(t) = 2V_{DC} \{Q_1(t) - Q_3(t)\} \quad (18)$$

$$Q_k(t) \in \{0, 1\}, \text{ where } k = 1, 2, \dots \quad (19)$$

Based on eqns. (18) and (19), the equations for the voltage of the primary [ $V_{LV}(t)$ ] and secondary [ $V_{HV}(t)$ ] bridges can be defined for the PSHPBD converter.

$$V_{LV}(t) = V_i(t) \{Q_1(t) - Q_3(t)\} \quad (20)$$

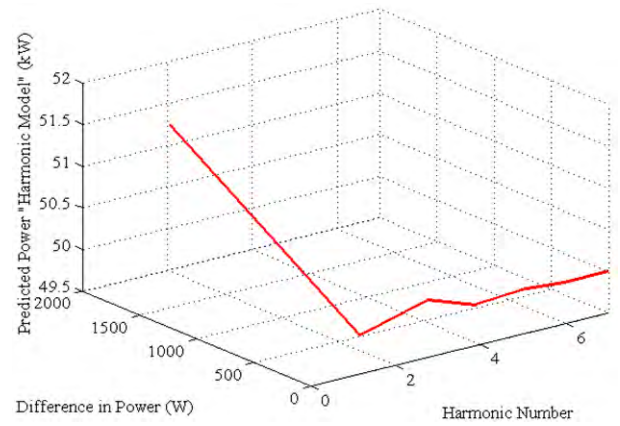


FIGURE 18. Relation between Harmonic number and power difference.

$$V_{HV}(t) = V_o(t) \{Q_5(t) - Q_7(t)\} \quad (21)$$

In Fig. 16 (a), on taking Kirchhoff Voltage Loop (KVL) summation across the converter, eqn. (22) is derived:

$$V_{LV}(t) - \frac{N_p}{N_s} V_{HV}(t) - R_L i_L(t) - L \frac{di_L(t)}{dt} = 0 \quad (22)$$

Using eqns. (20) and (21) in eqn. (22), it will be modified as given in eqn. (23)

$$L \frac{di_L(t)}{dt} + R_L i_L(t) = V_i(t) \{Q_1(t) - Q_3(t)\} - \frac{1}{n} V_o(t) \{Q_5(t) - Q_7(t)\} \quad (23)$$

In eqn. (23), the switching functions have binary values (0,1) and this switching function drives state variables ( $i_L$ ,  $V_c$ ) of the converter which are continuous in time. System/expression like these are classified as mixed mode dynamic system/expression because of the fact that both continuous and discrete time functions are included in the structure [40]. To simplify system like these, switching function is decomposed into its Fourier series components using harmonic modeling approach. Eqn. (24) is derived by applying Fourier transform to the switching square wave.

$$Q_k(t) = \frac{1}{2} + \frac{2}{\pi} \sum_{h=0}^H \frac{\sin([2h+1]\{\omega_s t - \lambda_k\})}{[2h+1]}, \quad \text{where; } H = 7, h = 1, 2, 3, \dots \quad (24)$$

where  $\omega_s$  is the square wave switching frequency (in rad/s) and  $k$  is the phase delay between reference phasor and square wave.

In the PSHPBD converter, there are eight (8) switches which forms four (4) sets/pairs, thus eqns. (25)-(28) expresses four switching functions for each leg of the converter.

$$Q_1(t) = \frac{1}{2} + \frac{2}{\pi} \sum_{h=0}^H \frac{\sin([2h+1]\{\omega_s t\})}{[2h+1]} \quad (25)$$

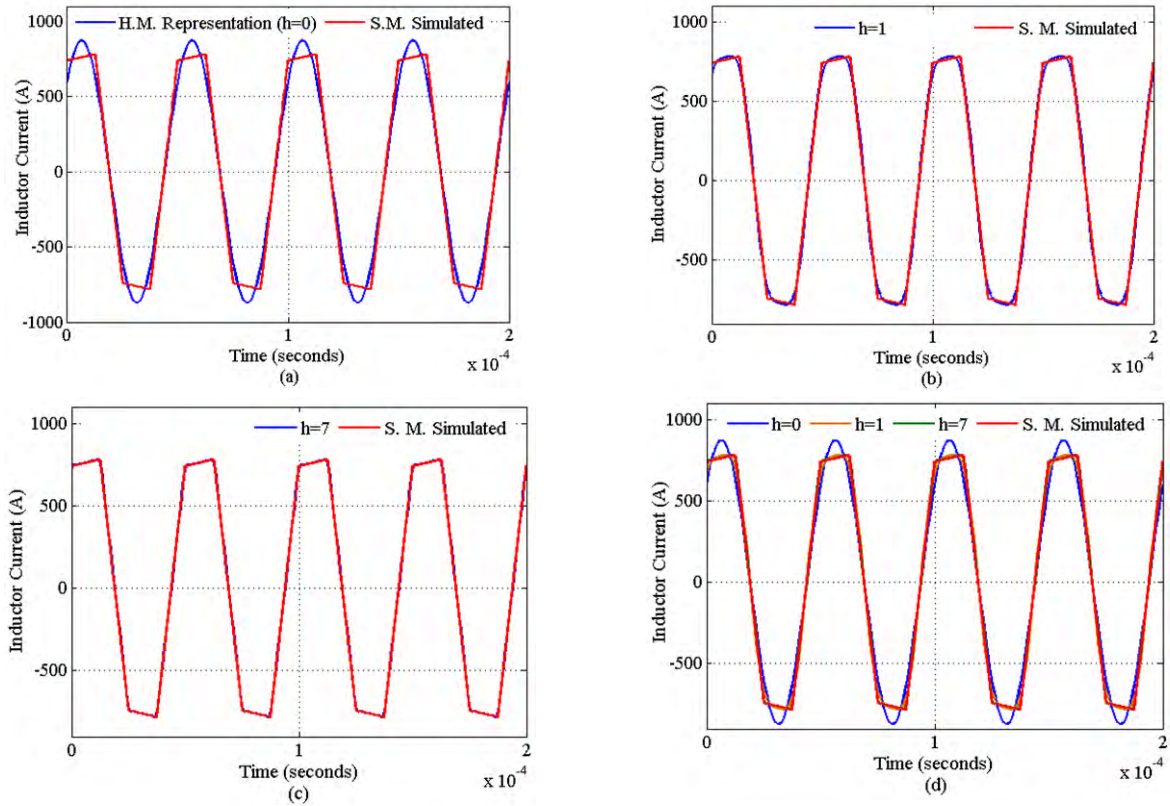


**FIGURE 19. Harmonic Model Verification for Inductor Current (in comparison with switched model simulation): (a) N (h = 0) Fundamental (b) N (h = 1) (c) N (h = 7) (d) N (h = 0, 1 and 7) all in one.**

$$Q_3(t) = \frac{1}{2} + \frac{2}{\pi} \sum_{h=0}^H \frac{\sin([2h+1]\{\omega_s t - \pi\})}{[2h+1]} \quad (26)$$

$$Q_5(t) = \frac{1}{2} + \frac{2}{\pi} \sum_{h=0}^H \frac{\sin([2h+1]\{\omega_s t - \delta\})}{[2h+1]} \quad (27)$$

$$Q_7(t) = \frac{1}{2} + \frac{2}{\pi} \sum_{h=0}^H \frac{\sin([2h+1]\{\omega_s t - \delta - \pi\})}{[2h+1]} \quad (28)$$

In eqns. (25)–(28), expression for  $Q_1$ ,  $Q_3$ ,  $Q_5$ ,  $Q_7$  are given whereas expression for  $Q_2$ ,  $Q_4$ ,  $Q_6$ ,  $Q_8$  can be derived similarly

$$P_{analytical} = \frac{1}{n} \frac{V_{in} V_{out}}{\omega L} \frac{\delta(\pi - |\delta|)}{\pi} \quad (29)$$

where,  $\delta$  is the phase shift between the two bridges

$$P_{harmonic\ model} = \frac{8}{\pi^2} V_{in} V_{out} \frac{1}{n} \sum_{h=0}^H \times \left\{ \frac{1}{[2h+1]^3} \frac{\sin([2h+1]\delta)}{\omega_s L} \right\} \quad (30)$$

$$P_{difference\ in\ pu} = \frac{P_{analytical} - P_{harmonic\ model}}{P_{analytical}} \quad (31)$$

as these are the complimentary functions of the first four functions expressed here. In the equations, “H” is the

harmonic number included in the expansion of the Fourier series for switching functions. In this paper, an optimal harmonic number “H” is selected for the parameters of the MEA Aircraft “X”. The optimal harmonic number “H” is selected by observing the match between the analytical power transfer equation given in eqn. (29) and the power transfer derived by the Fourier series expansion method, expressed in eqn. (30). The difference between the analytical power calculated by eqn. (29) and the harmonic model calculated by eqn. (30) is given in per unit in eqn. (31). Eqn. (31) helps in determining the optimal harmonic number “H”. In table 4, the values are given for different harmonic numbers (0 to 7). It is to be noted that for the case of MEA Aircraft “X”, the power transfer between the distribution architecture and the BESS is 50 kW, hence analytical power is 50000 W. For the same parameters, power transfer based on harmonic modeling is also calculated and given in table 4. It is to be observed that the power mismatch reduces as the harmonic number is increased. But, at the same time, a very high harmonic number cannot be taken as in that case the complexity will increase thus increasing the computational time. However, a very low harmonic number cannot be selected owing to the fact that the mismatch with the analytical power will be higher. Thus, very decisively an optimal harmonic number “H = 7” has been selected for the presented application. For H = 7, the power mismatch is 0.016 % (negative sign here



indicates that the power calculated by the harmonic model will be less than the analytical power). In comparison to harmonic number  $H = 6$ , the mismatch for  $H = 7$  is slightly higher but  $H = 7$  is selected as the mismatch is negative (referring Fig. 9, the margin on the lower side is 20 V and on the higher side it is only 10 V “250 – 280 V stability range for 270 V DC bus”). Fig. 18 shows the relation between harmonic number ( $H$ ), power calculated and power difference with the analytical power.

Finally, the state variables ( $i_L$  and  $V_c$ ) are derived using the harmonic modeling method. Eqn. (32), as shown at the bottom of the next page, gives the expression of the inductor current ( $i_L$ ) whereas expression for capacitor current ( $i_c$ ) is given in eqn. (33), as shown at the bottom of the next page. Using  $i_c$ , expression for the capacitor (output) voltage is derived ( $V_o$ ) and is given in eqn. (34), as shown at the bottom of the this page.

To confirm the modeling process, the inductor current predicted by eqn. (32) is matched to the results of the switched simulation in Fig. 19 (a)-(d). The figure shows that the inclusion of higher harmonics gives a more accurate representation of the AC inductor current waveform. In Fig. 19 (a),  $i_L$  for switch model based simulation (S.M.) and for harmonic model expression “H” i.e. “h” = 0 is shown. It is observed that the values of  $I_{pk}$  and  $I_r$  is not matching in the plot. Fig. 19 (b) shows the  $i_L$  for harmonic model representation H i.e. “h” = 1 and S.M. simulated case. It can be noticed that still, the values of  $I_{pk}$  and  $I_r$  are not matching in the plot. Fig. 19 (c) shows the  $i_L$  for harmonic model representation H i.e. “h” = 7 and S.M. simulated

case. It can be noticed from the figure, that the harmonic model waveform and switch model simulated waveform are coinciding and an accurate result is obtained. Fig 19 (d) shows the combined waveform for  $i_L$  for H.M. “h” = 0, 1, 7 and switch model simulated case. Harmonic number “h” = 7, is recorded closest/coinciding to the S.M. simulated waveform.

Similarly, Fig. 20 shows the match obtained for the case of capacitor current ( $i_c$ ), where although the prediction of the harmonic model (for “h” = 7) in Fig. 20 (c) still includes ripples due to the contribution of each harmonic component, it provides an excellent match to the simulated capacitor current. Figs. 20 (a) and (b) show the capacitor current ( $i_c$ ) for harmonic model representation H i.e. “h” = 0 and “h” = 1” respectively in comparison to the (S.M. simulated) case. It can be seen that there exist a big mismatch in the harmonic model and switch model. Fig. 20 (d) shows the combined waveform for  $i_c$  for H.M. “h” = 0, 1, 7 and S.M. simulated. Harmonic number “h” = 7, is recorded closest/coinciding to the S.M. simulated waveform with the presence of small ripples due to the contribution of each harmonic component.

The steady state output voltage expression ( $V_o$ ) obtained in eqn. (34) is verified in Fig. 21 (a) and (b) by comparing its result to that of the switched simulation. The error between these two waveforms exists when “h” = 1 as shown in Fig. 21 (a) whereas it is minimal for the case of “h” = 7 as shown in Fig. 3.15 (b). Figs. 19, 20 and 21 verifies the optimal number harmonic model for PSHPBD converter discussed in this section.

$$i_L(t) = \frac{4}{\pi} \sum_{h=0}^H \frac{1}{[2h+1]} \left\{ \frac{V_i(t)}{|Z[h]|} \sin([2h+1]\omega_s t - \varphi_Z[h]) - \frac{V_o(t)}{|Z[h]|} \frac{1}{n} \sin([2h+1](\omega_s t - \delta) - \varphi_Z[h]) \right\}; \quad (32)$$

$$\text{Where; } |Z[h]| = \sqrt{R_L^2 + ([2h+1]\omega_s L)^2} \quad \text{and } \varphi_Z[h] = \tan^{-1} \left( \frac{[2h+1]\omega_s L}{R_L} \right) \quad (33)$$

$$I_c(t) = -i_{load}(t) + \frac{8}{C\pi^2} \frac{1}{n_t} \sum_{n=0}^H \sum_{m=0}^H \frac{1}{[2n+1][2m+1]} \left\{ \begin{aligned} & \frac{V_{in}}{|Z[m]|} \left[ \cos \left\{ \begin{aligned} & [2n+1](\omega_s t - \delta) \\ & - [2m+1]\omega_s t + \phi_z[m] \end{aligned} \right\} \right. \\ & \left. - \cos \left\{ \begin{aligned} & [2n+1](\omega_s t - \delta) \\ & - [2m+1]\omega_s t - \phi_z[m] \end{aligned} \right\} \right] \\ & - \frac{1}{n_t} \frac{V_{out}(t)}{|Z[m]|} \left[ \cos \left\{ \begin{aligned} & [2n+1](\omega_s t - \delta) \\ & - [2m+1](\omega_s t - \delta) + \phi_z[m] \end{aligned} \right\} \right. \\ & \left. - \cos \left\{ \begin{aligned} & [2n+1](\omega_s t - \delta) \\ & - [2m+1](\omega_s t - \delta) - \phi_z[m] \end{aligned} \right\} \right] \end{aligned} \right\} \quad (34)$$

$$\frac{dV_o(t)}{dt} = \frac{i_c(t)}{C} = -i_{load}(t) + \frac{8}{C\pi^2} \frac{1}{n_t} \sum_{n=0}^H \sum_{m=0}^H \frac{1}{[2n+1][2m+1]} \times \left\{ \begin{aligned} & \frac{V_{in}}{|Z[m]|} \left[ \cos \{ [2n+1](\omega_s t - \delta) - [2m+1]\omega_s t + \phi_z[m] \} \right. \\ & \left. - \cos \{ [2n+1](\omega_s t - \delta) - [2m+1]\omega_s t - \phi_z[m] \} \right] \\ & - \frac{1}{n_t} \frac{V_{out}(t)}{|Z[m]|} \left[ \cos \{ [2n+1](\omega_s t - \delta) - [2m+1](\omega_s t - \delta) + \phi_z[m] \} \right. \\ & \left. - \cos \{ [2n+1](\omega_s t - \delta) - [2m+1](\omega_s t - \delta) - \phi_z[m] \} \right] \end{aligned} \right\} \quad (35)$$

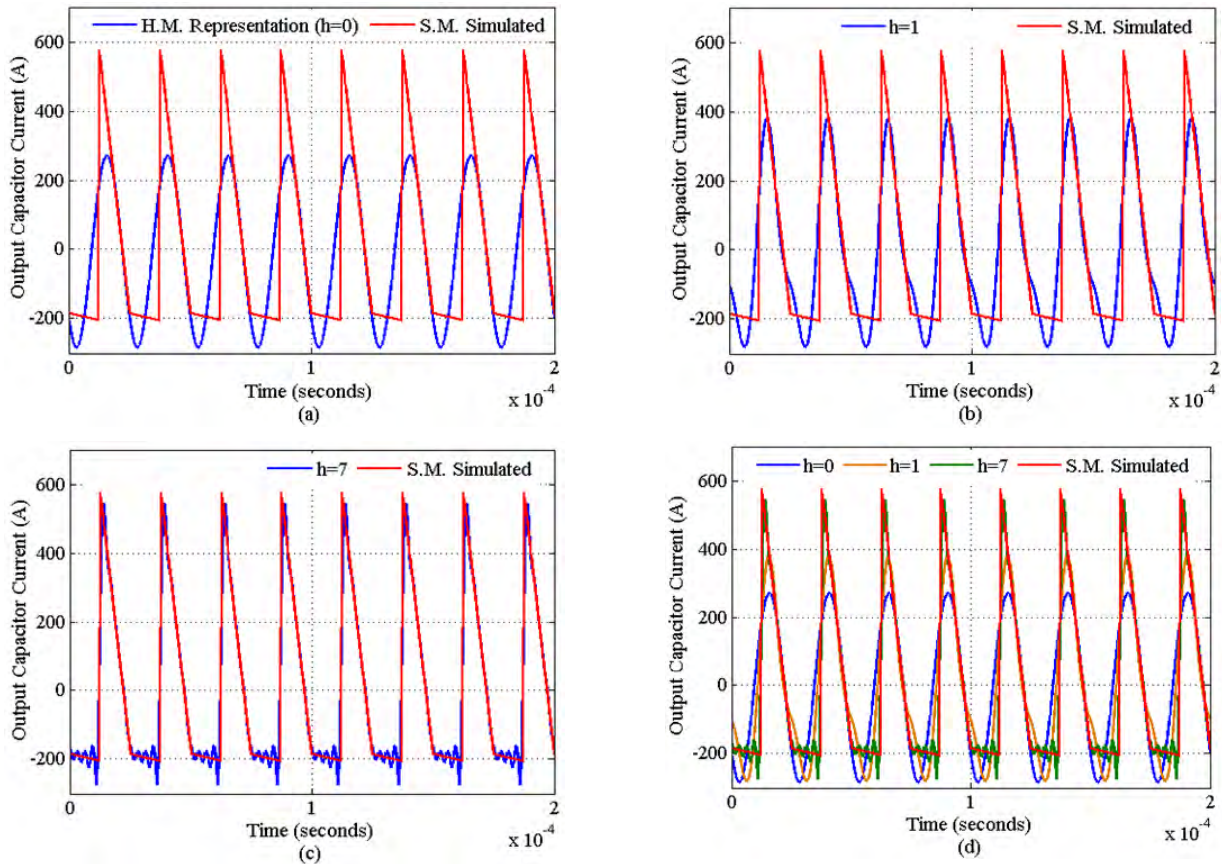


**FIGURE 20.** Harmonic Model Verification for Output Capacitor Current (in comparison with switched model simulation): (a)  $N(h=0)$  Fundamental (b)  $N(h=1)$  (c)  $N(h=7)$  (d)  $N(h=0,1,7)$  all in one.

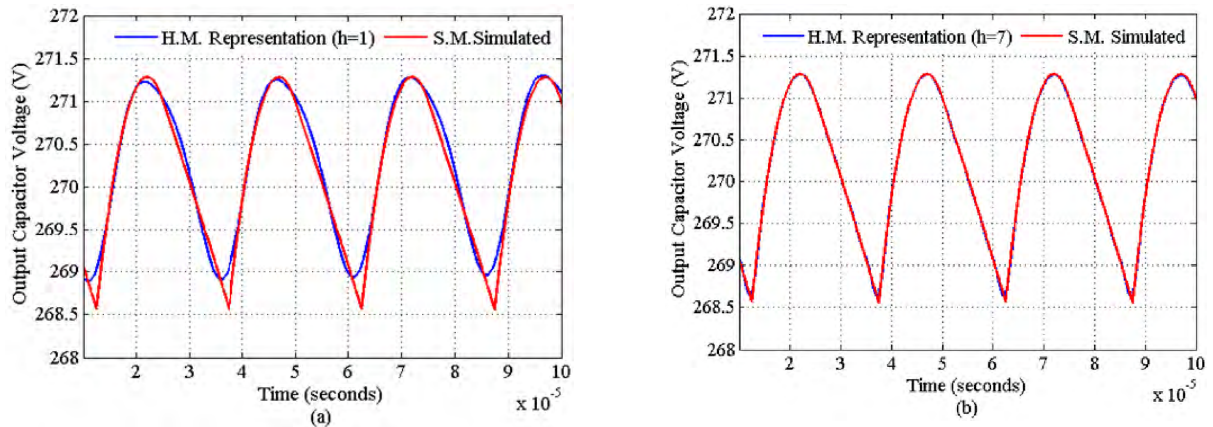


**FIGURE 21.** Harmonic Model Verification for Output Capacitor Voltage (in comparison with switched model simulation): (a)  $N(h=1)$  (b)  $N(h=7)$ .

## V. BESS INTEGRATION TO THE MEA 270 V DC ARCHITECTURE USING PREDICTIVE PEAK CURRENT CONTROL TECHNIQUE

In this section, the proposed BESS is integrated with the MEA Aircraft “X” 270 V DC power distribution network. A predictive peak current based control technique is proposed for the integration. It is a fast response controller owing to the removal of PI regulator in both i.e. the outer

voltage loop as well as in the inner current loop. As shown in Fig. 22, the outer voltage control loop is replaced by the prediction technique and the inner current control loop is replaced by the comparison of the actual current and the predicted current. With this, the current control loop theoretically has the bandwidth equal to the switching frequency of the PSHPBD converter. The proposed fast response control technique is based on the direct estimation/prediction

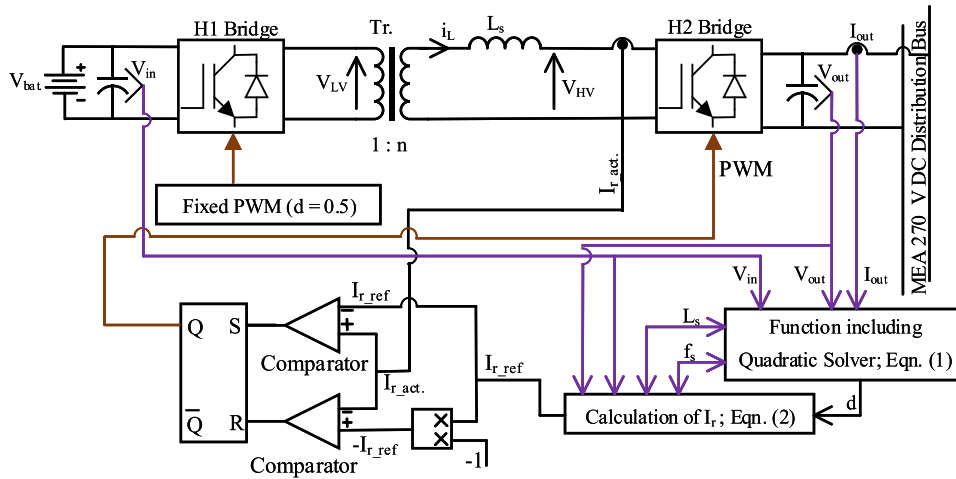


**FIGURE 22.** Proposed predictive peak current control technique for integration of the PSHPBD converter in MEA.

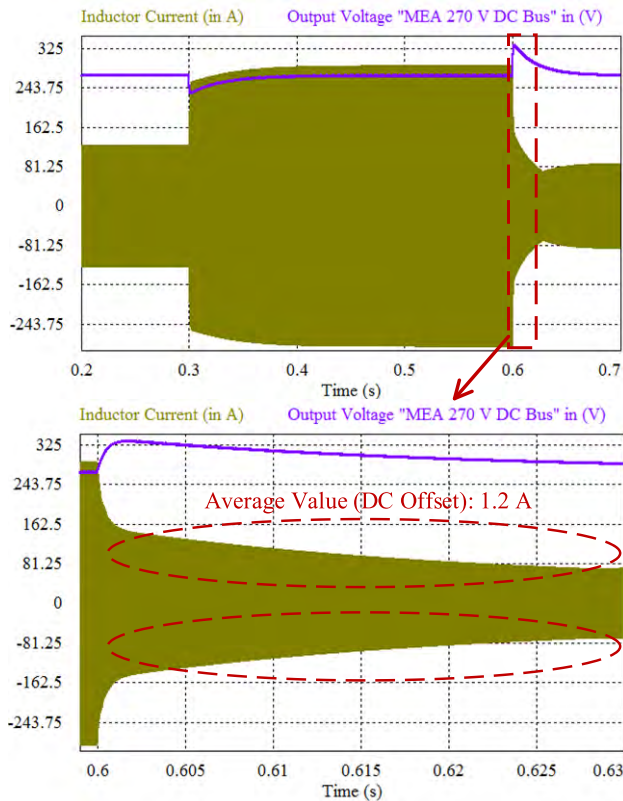


**FIGURE 23.** Conventional PI-based control step-response in output voltage and inductor current.

of the duty cycle “ $d$ ” which is dependent on input voltage, output current, transformer turns ratio, coupled inductance and the switching frequency from eqn. (11). The duty cycle “ $d$ ” is calculated using quadratic solver approach. The calculated “ $d$ ” is further used in the calculation of the reference current  $I_r$  from eqn. (10) which corresponds to the switching of the secondary bridge switches as seen

**TABLE 4.** Power difference between harmonic model and analytical.

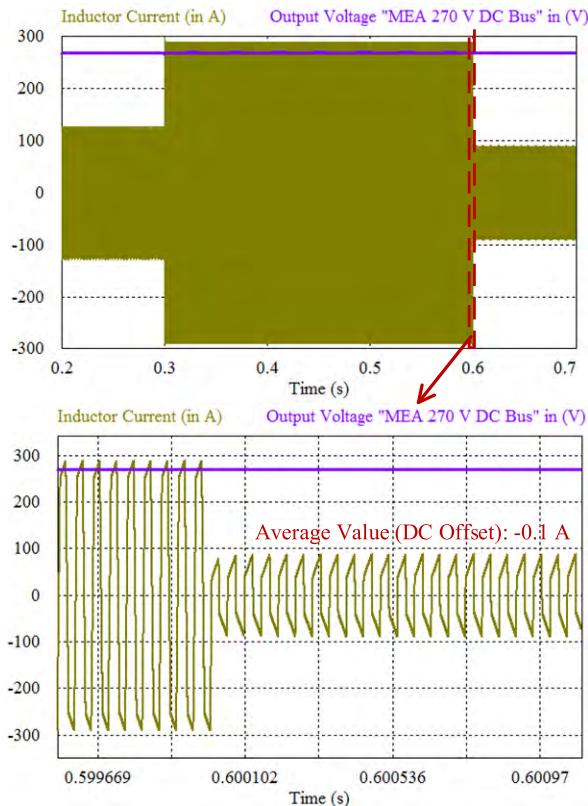
Harmonic No.	Analytical Power (W)	Harmonic Model Power (W)	Difference in Power (W)	Relative Error (p.u.)
0	50000	51600.46	1600.46	0.03201
1	50000	49689.33	310.67	-0.00621
2	50000	50102.14	102.14	0.00204
3	50000	49951.70	48.30	-0.00097
4	50000	50022.48	22.48	0.00045
5	50000	49983.71	16.29	-0.00033
6	50000	50007.20	7.20	0.00014
7	50000	49991.91	8.09	-0.00016
7	20000	19993.35	6.65	-0.00033
7	10000	9989.80	10.20	-0.00102

in Fig. 16 (b) and observed from the different cases given in table 5. In the proposed control structure, the primary bridge is supplied (driven) by a fixed 50 % duty ratio signal whereas the secondary bridge is also driven by the fixed 50 % duty ratio signal but with a phase shift. The phase shift value is dependent on the time duration required for the “ $i_L$ ” (inductor current) to reach the predefined specified reference value ( $I_r$ ) current of the inductor. From Fig. 16 (b), the inductor current has two values of  $I_r$  in a cycle i.e. this current instant occurs twice in every cycle thus making the proposed control to operate on cycle by cycle basis. This cycle by cycle operation makes the controller respond to changes in the reference command within a cycle thus making it a fast response controller. Since the “ $I_r$ ” has two instants in a cycle (positive and negative) the discussed control technique will produce symmetrical current (dc offset = 0) on the transformer windings which will avoid the saturation of the transformer core.



**TABLE 5.** Switch logic for the secondary side switches ( $S_5, S_6$  forms one leg and  $S_7, S_8$  forms another leg as seen in fig. (16.a)).

Conditions	Time	S	R	Q	Switch State
Case 1	$t_1 - t_2$	$I_{r\_act} > I_{r\_ref}; S = 1$	$I_{r\_act} > -I_{r\_ref}; R = 0$	$Q = 1$	$S_5$ and $S_8$ will be ON; $S_6$ and $S_7$ will be Off
Case 2	$t_2 - t_3$	$I_{r\_act} < I_{r\_ref}; S = 0$	$I_{r\_act} > -I_{r\_ref}; R = 0$	$Q = 1$	$S_5$ and $S_8$ will be ON; $S_6$ and $S_7$ will be Off
Case 3	$t_3 - t_4$	$I_{r\_act} < I_{r\_ref}; S = 0$	$I_{r\_act} < -I_{r\_ref}; R = 1$	$Q = 0$	$S_6$ and $S_7$ will be ON; $S_5$ and $S_8$ will be Off
Case 4	$t_4 - t_5$	$I_{r\_act} < I_{r\_ref}; S = 0$	$I_{r\_act} > -I_{r\_ref}; R = 0$	$Q = 0$	$S_6$ and $S_7$ will be ON; $S_5$ and $S_8$ will be Off

**FIGURE 24.** Proposed predicted peak current based fast response control step-response in output voltage and inductor current.

The control structure shown in Fig. 22, is verified by the simulation. The performance of the proposed predicted peak current based fast response control structure is compared with the state of the art “conventional” dual loop control having a PI regulator. The comparative results are captured, presented and discussed here. The output voltage and inductor current response for the case of conventional dual loop controller are shown in Fig. 23. A high impulse response is observed in the output voltage waveform at the load change point at 0.3s and 0.6s. As observed in Fig. 23 from the transient situation shown for inductor current, the output voltage is regulated after many switching cycles. The settling time shown in Fig. 23 is from 0.6s to 0.63s. In Fig. 24, the output voltage and the inductor current response for the step change in load is shown for the case of the proposed predicted peak current based fast response control structure. The output voltage is regulated within a cycle (0.6s to 0.6001s) as is evident from the waveform of the inductor current shown in Fig. 24.

Thus the claim for fast response is verified by the simulation results. Moreover, it is also observed that the average current (dc offset) of the coupling inductor (transformer secondary winding) for the peak current control case is approx. zero ( $-0.1$  A), whereas for the conventional control it is 1.02 A as seen from Fig. 24 and Fig. 23 respectively. There will be zero DC offset in the transformer windings and the DC magnetization will be eliminated thus avoiding the saturation of the transformer core as the average current is zero in the case of predicted peak current based fast response control structure.

## VI. CONCLUSION

In this paper, the electrical loads in the MEA has been explained in detail to understand the requirements for the battery energy storage system. Based on the requirements, a 6.4 k Watt-hour, 50 k Watt battery system was designed for the MEA Aircraft “X”. The designed battery system was modeled and compared with the inbuilt model in MATLAB<sup>®</sup> with satisfactory results. Similarly, the battery charger was also designed and modeled using an optimal harmonic number ( $h = 7$ ), showing the relative error of only 0.016% with the analytical results. Finally, the BESS was integrated with the MEA Aircraft “X” 270 V DC power distribution architecture using the novel predicted peak current based fast response controller. A better transient response with peak current limited to the predefined value of the inductor peak current has been observed for the case of discussed control technique. The suitability of the proposed control for the MEA with respect to the response time has also been presented. It has also been found out that with the proposed control technique the DC offset current is zero which will avoid the transformer core from saturation, thus increasing the life of the battery charger in particular and the BESS in general.

## REFERENCES

- [1] IATA Forecasts Passenger Demand to Double Over 20 Years. Assessed: Jul. 10, 2017. [Online]. Available: <http://www.iata.org/pressroom/pr/Pages/2016-10-18-02.aspx>
- [2] P. Nuzzo et al., “A contract-based methodology for aircraft electric power system design,” *IEEE Access*, vol. 2, pp. 1–25, 2014.
- [3] B. Sarlioglu and C. T. Morris, “More electric aircraft: Review, challenges, and opportunities for commercial transport aircraft,” *IEEE Trans. Transp. Electric.*, vol. 1, no. 1, pp. 54–64, Jun. 2015.
- [4] M. Tariq, A. I. Maswood, A. C. Moreddy, C. J. Gajanayake, M. Y. Lee, and A. K. Gupta, “Reliability, dead-time, and feasibility analysis of a novel modular tankless ZCS inverter for more electric aircraft,” *IEEE Trans. Transp. Electric.*, vol. 3, no. 4, pp. 843–854, Dec. 2017.
- [5] R. I. Jones, “The more electric aircraft: The past and the future?” in *Proc. IEE Colloq. Elect. Mach. Syst. Electr. Aircr.*, London, U.K., 1999, pp. 1–1–1–4.



- [6] G. Buticchi, L. Costa, and M. Liserre, "Improving system efficiency for the more electric aircraft: A look at DC/DC converters for the avionic onboard DC microgrid," *IEEE Ind. Electron. Mag.*, vol. 11, no. 3, pp. 26–36, Sep. 2017.
- [7] A. Fotouhi, D. J. Auger, K. Propp, and S. Longo, "Electric vehicle battery parameter identification and SOC observability analysis: NiMH and Li-S case studies," *IET Power Electron.*, vol. 10, no. 11, pp. 1289–1297, 2017.
- [8] J. Jaguemont, L. Boulon, and Y. Dube, "Characterization and modeling of a hybrid-electric-vehicle lithium-ion battery pack at low temperatures," *IEEE Trans. Veh. Technol.*, vol. 65, no. 1, pp. 1–14, Jan. 2016.
- [9] A. Mohammadi, D. Rekioua, T. Rekioua, and S. Bacha, "Valve regulated lead acid battery behavior in a renewable energy system under an ideal mediterranean climate," *Int. J. Hydrogen Energy*, vol. 41, no. 45, pp. 20928–20938, 2016.
- [10] S. Vavilapalli, U. Subramaniam, S. Padmanaban, and V. K. Ramachandramurthy, "Design and real-time simulation of an AC voltage regulator based battery charger for large-scale PV-grid energy storage systems," *IEEE Access*, vol. 5, pp. 25158–25170, 2017.
- [11] U. Akram, M. Khalid, and S. Shafiq, "An innovative hybrid wind-solar and battery-supercapacitor microgrid system—Development and optimization," *IEEE Access*, vol. 5, pp. 25897–25912, 2017.
- [12] S. Lee, J. Kim, J. Lee, and B. H. Cho, "State-of-charge and capacity estimation of lithium-ion battery using a new open-circuit voltage versus state-of-charge," *J. Power Sources*, vol. 185, no. 2, pp. 1367–1373, 2008.
- [13] M. Charkgard and M. Farrokhi, "State-of-charge estimation for lithium-ion batteries using neural networks and EKF," *IEEE Trans. Ind. Electron.*, vol. 57, no. 12, pp. 4178–4187, Dec. 2010.
- [14] D. Di Domenico, A. Stefanopoulou, and G. Fiengo, "Lithium-ion battery state of charge and critical surface charge estimation using an electrochemical model-based extended Kalman filter," *J. Dyn. Syst., Meas., Control*, vol. 132, no. 6, p. 061302, 2010.
- [15] X. Hu, J. Jiang, D. Cao, and B. Egardt, "Battery health prognosis for electric vehicles using sample entropy and sparse Bayesian predictive modeling," *IEEE Trans. Ind. Electron.*, vol. 63, no. 4, pp. 2645–2656, Apr. 2016.
- [16] C. Zou, X. Hu, Z. Wei, and X. Tang, "Electrothermal dynamics-conscious lithium-ion battery cell-level charging management via state-monitored predictive control," *Energy*, vol. 141, pp. 250–259, Dec. 2017.
- [17] Z. Wang, J. Ma, and L. Zhang, "Finite element thermal model and simulation for a cylindrical Li-ion battery," *IEEE Access*, vol. 5, pp. 15372–15379, 2017.
- [18] C. Zou, X. Hu, S. Dey, L. Zhang, and X. Tang, "Nonlinear fractional-order estimator with guaranteed robustness and stability for lithium-ion batteries," *IEEE Trans. Ind. Electron.*, vol. 65, no. 7, pp. 5951–5961, Jul. 2018.
- [19] L. Zhang, X. Hu, Z. Wang, F. Sun, J. Deng, and D. G. Dorrell, "Multiobjective optimal sizing of hybrid energy storage system for electric vehicles," *IEEE Trans. Veh. Technol.*, vol. 67, no. 2, pp. 1027–1035, Feb. 2018.
- [20] H. Qin and J. W. Kimball, "Generalized average modeling of dual active bridge DC–DC converter," *IEEE Trans. Power Electron.*, vol. 27, no. 4, pp. 2078–2084, Apr. 2012.
- [21] R. T. Naayagi, A. J. Forsyth, and R. Shuttleworth, "High-power bidirectional DC–DC converter for aerospace applications," *IEEE Trans. Power Electron.*, vol. 27, no. 11, pp. 4366–4379, Nov. 2012.
- [22] H. Bai, Z. Nie, and C. C. Mi, "Experimental comparison of traditional phase-shift, dual-phase-shift, and model-based control of isolated bidirectional DC–DC converters," *IEEE Trans. Power Electron.*, vol. 25, no. 6, pp. 1444–1449, Jun. 2010.
- [23] Y.-C. Wang, Y.-C. Wu, and T.-L. Lee, "Design and implementation of a bidirectional isolated dual-active-bridge-based DC/DC converter with dual-phase-shift control for electric vehicle battery," in *Proc. IEEE Energy Convers. Congr. Expo. (ECCE)*, Sep. 2013, pp. 5468–5475.
- [24] K. Wu, C. W. de Silva, and W. G. Dunford, "Stability analysis of isolated bidirectional dual active full-bridge DC–DC converter with triple phase-shift control," *IEEE Trans. Power Electron.*, vol. 27, no. 4, pp. 2007–2017, Apr. 2012.
- [25] B. Zhao, Q. Yu, and W. Sun, "Extended-phase-shift control of isolated bidirectional DC–DC converter for power distribution in microgrid," *IEEE Trans. Power Electron.*, vol. 27, no. 11, pp. 4667–4680, Nov. 2012.
- [26] A. A. Abdelhafez and A. J. Forsyth, "A review of more-electric aircraft," in *Proc. 13th Int. Conf. Aerosp. Sci. Aviation Technol. (ASAT)*, 2009, pp. 1–13, Paper ASAT-13-EP-01.
- [27] M. Tariq, A. I. Maswood, C. J. Gajanayake, and A. K. Gupta, "Aircraft batteries: Current trend towards more electric aircraft," *IET Elect. Syst. Transp.*, vol. 7, no. 2, pp. 93–103, 2017.
- [28] C. I. Hill, S. Bozhko, T. Yang, P. Giangrande, and C. Gerada, "More electric aircraft electro-mechanical actuator regenerated power management," in *Proc. IEEE 24th Int. Symp. Ind. Electron. (ISIE)*, Buzios, Brazil, Jun. 2015, pp. 337–342.
- [29] S. N. Motapon, L.-A. Dessaint, and K. Al-Haddad, "A robust H<sub>2</sub>-consumption-minimization-based energy management strategy for a fuel cell hybrid emergency power system of more electric aircraft," *IEEE Trans. Ind. Electron.*, vol. 61, no. 11, pp. 6148–6156, Nov. 2014.
- [30] S. R. MacMinn and W. D. Jones, "A very high speed switched-reluctance starter-generator for aircraft engine applications," in *Proc. IEEE Nat. Aerosp. Electron. Conf.*, Dayton, OH, USA, vol. 4, May 1989, pp. 1758–1764.
- [31] E. Chemali, M. Preindl, P. Malysz, and A. Emadi, "Electrochemical and electrostatic energy storage and management systems for electric drive vehicles: State-of-the-art review and future trends," *IEEE J. Emerg. Sel. Topics Power Electron.*, vol. 4, no. 3, pp. 1117–1134, Sep. 2016.
- [32] (2004). *Military Standard, Aircraft Electric Power Characteristics MIL-STD-704F*. [Online]. Available: [https://prod.nais.nasa.gov/eps/eps\\_data/137899-SOL-001-015.pdf](https://prod.nais.nasa.gov/eps/eps_data/137899-SOL-001-015.pdf)
- [33] X. Roboam, B. Sareni, and A. D. Andrade, "More electricity in the air: Toward optimized electrical networks embedded in more-electrical aircraft," *IEEE Ind. Electron. Mag.*, vol. 6, no. 4, pp. 6–17, Dec. 2012.
- [34] D. S. Lee et al., "Transport impacts on atmosphere and climate: Aviation," *Atmos. Environ.*, vol. 44, no. 37, pp. 4678–4734, 2010.
- [35] M. Kaufmann, D. Zenkert, and C. Mattei, "Cost optimization of composite aircraft structures including variable laminate qualities," *Compos. Sci. Technol.*, vol. 68, no. 13, pp. 2748–2754, 2008.
- [36] M. Kaufmann, D. Zenkert, and P. Wennhage, "Integrated cost/weight optimization of aircraft structures," *Struct. Multidisciplinary Optim.*, vol. 41, no. 2, pp. 325–334, 2010.
- [37] EaglePicher Technologies, LLC. *MAR-9526 High Power Battery Datasheet: Lithium-Ion—Iron Phosphate (LFP) Chemistry Rechargeable*. Assessed: Mar. 10, 2016. [Online]. Available: <http://www.eaglepicher.com/images/Li-Ion/EP%20MAR%209526%20LITHIUM%20ION%20DATA%20SHEET.PDF>
- [38] S. N. Motapon, L.-A. Dessaint, and K. Al-Haddad, "A comparative study of energy management schemes for a fuel-cell hybrid emergency power system of more-electric aircraft," *IEEE Trans. Ind. Electron.*, vol. 61, no. 3, pp. 1320–1334, Mar. 2014.
- [39] R. W. A. A. De Doncker, D. M. Divan, and M. H. Kheraluwala, "A three-phase soft-switched high-power-density DC/DC converter for high-power applications," *IEEE Trans. Ind. Appl.*, vol. 27, no. 1, pp. 63–73, Jan. 1991.
- [40] D. Segaran, D. G. Holmes, and B. P. McGrath, "Enhanced load step response for a bidirectional DC–DC converter," *IEEE Trans. Power Electron.*, vol. 28, no. 1, pp. 371–379, Jan. 2013.



**MOHD TARIQ** (S'10) received the bachelor's degree in electrical engineering from Aligarh Muslim University and the master's degree in machine drives and power electronics from IIT Kharagpur. He is currently pursuing the Ph.D. degree from Nanyang Technological University, Singapore. He has been a scientist with NIOT (an autonomous institute), Chennai, under the Ministry of Earth Sciences, Government of India, and was also an Assistant Professor with the National Institute of Technology, Bhopal, India. He is currently with the Rolls-Royce@NTU Corporate Lab, where he is involved on the technologies related to more electric aircraft.

His research interest includes power converters, and energy storage devices and its optimal control for the electrified transportation and renewable energy application. He is a recipient of the best paper award from the IEEE Industrial Applications Society's and the Industrial Electronic Society, Malaysia Section—Annual Symposium (ISCAIE-2016), Penang, Malaysia.



**ALI I. MASWOOD** (SM'96) received the B.Eng. and M.Eng. degrees (Hons.) from the Moscow Power Engineering Institute and the Ph.D. degree from Concordia University, Montreal, Canada. Having taught in Canada for a number of years, he joined Nanyang Technological University, Singapore, in 1991, where he is currently an Associate Professor.

His research interest is in power electronics, particularly in converter generated harmonics, novel inverter topology, advanced PWM switching, and power quality. He has authored several International Journal and Conference publications on these topics. He is also the chapter-author *Power Electronics, Handbook* (San Diego, USA: Academic Press, 2002). His work in FROSIN switch mode power supply gave rise to several patents. He is actively involved in the local IAS/PELS chapter and in the steering committee of the IEEE Power Electronics and Drives Conference.



**CHANDANA JAYAMPATHI GAJANAYAKE** (S'07–M'09–SM'13) received the B.Sc. degree in electrical and electronic engineering from the University of Peradeniya, Peradeniya, Sri Lanka, in 2003, and the Ph.D. degree in electrical and electronic engineering from Nanyang Technological University, Singapore, in 2008. In 2006, he was a Visiting Scholar with the Institute of Energy Technology, Aalborg University, Aalborg, Denmark. In 2008, he joined the Laboratory for Clean

Energy Research, School of Electrical and Electronic Engineering, Nanyang Technological University, as a Research Fellow. He is currently with the Applied Capability Group, Rolls-Royce Singapore Pte Ltd., Singapore. His research interests include power converters, machine drives, power quality, and distributed generation and microgrid energy management. He is a member of the IEEE Power Electronics Society and the Power and Energy Society.



**AMIT K. GUPTA** (S'04–M'08–SM'12) received the bachelor's degree in electrical engineering from IIT Roorkee and the Ph.D. degree in electrical engineering from the National University of Singapore. From 2000 to 2012, he was with Bechtel Corporation, Samsung Heavy Industries, Delphi Automotive Systems, and Vestas Wind Systems. Since 2012, he has been the Chief of Electrical Capability Group, Rolls-Royce Singapore Pte Ltd. He is currently the Head of the

Electrical Programme, Rolls-Royce@NTU Corporate Lab.

He is currently an Adjunct Professor with ECE, NUS and EEE, NTU. To date he has been granted 22 patents and filed another 21 patents. He has also published over 70 papers in international conferences and journals. He holds a six sigma Green Belt Certificate from Delphi Automotive Systems and trained in six sigma Black Belt techniques through Vestas Wind Systems.

He received the 2016 IEEE R10 Industry-Academia collaboration award for developing world class electrical R&T lab EPSIL@N. He was runner up in the 2015 Rolls-Royce Engineering and Technology Technical Awards. He is a recipient of the Vestas Innovation Excellence Award for being top five innovators of Vestas Global Research. He is a recipient of the Prize paper from the IEEE Industrial Applications Society's-Industrial Power Converter Committee in 2005.

He is Fellow of the IET and a Chartered Engineer from Engineering Council, U.K. He is an Associate Editor for the IEEE TRANSACTIONS ON POWER ELECTRONICS and plays an active role in organizing electrical power engineering conferences in Asia.

...